A Computational and Experimental Study of Ta$_2$O$_5$ Thin Films

Sanjayan Sathasivam[a,b], Benjamin A. D. Williamson[c], Andreas Kafizas[a], Shaeel A. Althabaiti[d,e], Abdullah Y. Obaid[,e], Sulaiman N. Basahel[d,e], David O. Scanlon[c,f], Claire J. Carmalt[a] and Ivan P. Parkin[a]*

*Corresponding author

[a]Materials Chemistry Centre, Department of Chemistry, University College London, 20 Gordon Street, London WC1H 0AJ, UK

Fax: (+44) 20-7679-7463

E-mail: i.p.parkin@ucl.ac.uk

[b]Bio Nano Consulting Ltd, The Gridiron Building, One Pancras Square, London N1C 4AG, UK

Fax: (+44) 20-7396-1056

E-mail: info@bio-nano-consulting.com

[c]Kathleen Lonsdale Materials Chemistry, Department of Chemistry, University College London, 20 Gordon Street, London WC1H 0AJ, U.K.

[d]Chemistry Department, King Abdulaziz University, Saudi Arabia

[e]Surface Chemistry and Catalytic Studies Group, King Abdulaziz University, Saudi Arabia

[f] Diamond Light Source Ltd., Diamond House, Harwell Science and Innovation Campus, Didcot, Oxfordshire OX11 0DE, United Kingdom.

Abstract

This paper reports the novel synthesis of amorphous Ta$_2$O$_5$, and the subsequent isolation of the orthorhombic (β) crystallographic phase, using aerosol assisted chemical vapor deposition. Hybrid density functional theory was used to obtain the calculated optical band gap (3.83 eV) for the first time, which closely matches our experimental findings (3.85 eV). The films were highly transparent in the visible and

near IR region of the electromagnetic spectrum. The refractive indexes, calculated using the Swanepoel method, showed good agreement with literature findings. The photocatalytic properties of the films, determined through the photominerilisation of stearic acid under 254 nm radiation showed the amorphous sample to be an order of magnitude superior over crystalline β-Ta_2O_5.

Introduction

Tantalum oxide (Ta_2O_5) is an important wide band gap material with interesting structural and functional properties allowing it to have a wide range of applications.[1] It is a well-known high-κ (>20) dielectric material with a low leakage current that is used in commercial high-density capacitors for dynamic random access memory (DRAM) applications.[2–4] Amorphous Ta_2O_5 films, as gate oxides, provide insufficient protection against current leakage, primarily due to organic impurities or oxygen vacancies that give rise to the Frenkel-Pool effect taking place. Therefore, only crystalline films are usually employed for gate oxide applications.[5] Amorphous Ta_2O_5 can however (as well as the crystalline form) be used as a photocatalyst, in particular for the splitting of water for producing H_2 fuel, despite its wide band gap of ~4.0 eV at room temperature.[6–8] However, when doped with nitrogen the band gap of Ta_2O_5 has been reported to be reduced to as low as 2.4 eV (at RT) to allow activation using visible light for photocatalytic water splitting, reduction of CO_2 and photo assisted *p*-type conductivity.[9,10] In addition to this, Ta_2O_5 has found use in optical and anti corrosion coatings.[11–13]

As well as its multifunctional properties, Ta_2O_5 also has interesting structural properties. It is amorphous at temperatures below 650 ^{o}C but when crystalline, can exist in many forms including those that are deficient and rich in oxygen.[11,14] There is a distinct phase transition at 1360 ^{o}C from the low temperature (L) crystalline phase to a high temperature (H) crystalline phase. The exact crystal structure of these phases is still yet to be fully determined, primarily due the difficultly in growing stable single crystals of Ta_2O_5, even when stabilized with other metal oxides. Most recent advances into the structure of Ta_2O_5 have proposed an orthorhombic arrangement of the L temperature form (β-Ta_2O_5) as well as a less common phase consisting of a hexagonal (δ-Ta_2O_5) unit cell has also been suggested.[15–19] The H-Ta_2O_5 phase is not fully resolved with orthorhombic, tetragonal and monoclinic unit cells suggested.[11,20]

Ta$_2$O$_5$ has been synthesised by a wide range of techniques ranging from the simple chemical or oxidation of Ta metal[21] to high vacuum physical vapor deposition (PVD) methods such as radio frequency sputtering.[22–24] Chemical vapor deposition (CVD) is also extensively employed to obtain films from precursors such as Ta(OEt)$_5$[1] and from the metal halides - TaI$_5$[25], TaCl$_5$[26] and TaF$_5$[3]. The fabrication technique (as well as substrate identity and post deposition annealing) has often been strongly related to film properties.[14]

Here we present a novel route to amorphous Ta$_2$O$_5$ (with subsequent crystallization and isolation of the low temperature β phase *via* an annealing step in air.). This was achieved using a specialized form of CVD, called aerosol assisted chemical vapor deposition (AACVD), and is the first instance in which Ta$_2$O$_5$ has been grown by this technique.[27–30] This simple, cost effective and easily scalable technique operates at atmospheric pressure and relies on the transport of precursors into the deposition chamber *via* an aerosol mist.[31–33] AACVD places no volatility limitation on the precursors, the only condition being that they dissolve in a given solvent that can be vaporized.[34,35]

Experimental

Deposition Procedure

Depositions were carried out in N$_2$ (BOC Ltd., oxygen free nitrogen, 99.99% purity). Ta(OEt)$_5$ precursor (99%) was placed in a glass bubbler along with dry methanol and an aerosol mist created using a piezoelectric device (Johnson Matthey liquifog®). Ta(OEt)$_5$ procured from Aldrich and used as received. MeOH was also procured from Aldrich but dried over Mg and stored under molecular sieves before use.

Ta(OEt)$_5$ (0.5 g, 1.23 mmol) was dissolved in MeOH (20 ml). The resulting solution was stirred for 10 minutes and then atomised. The precursor vapour was carried to the reactor using a constant N$_2$ flow of 0.5 L.min^{-1}. Films were grown on quartz slides placed on SiO$_2$ barrier coated float glass (Pilkington NSG). A top plate was suspended 0.5 cm above the glass substrate to ensure laminar flow. The deposition was conducted at 450 °C, where the substrate was heated on its underside using cartridge heaters embedded within a graphite block. The reaction took 60 minutes to complete.

After the deposition the bubblers were closed and the substrates were cooled under a flow of N_2. The glass substrate was allowed to cool with the graphite block to less than 100 °C before it was removed. Coated substrates were handled and stored in air. The coated glass substrate was cut into ca. 1 cm × 1 cm squares for subsequent analysis.

Annealing Procedure

The Ta_2O_5 films on quartz were annealed in a Carbolite GLM 1 furnace with a Eurotherm 2216e temperature controller in air. Films were placed inside the oven at room temperature and heated to 1000 °C, at a rate of 10 °C per minute, before being held at this temperature for 12 hrs. The furnace was allowed to cool to below 100 °C before film was removed.

Film Characterisation

X-ray diffraction (XRD) patterns were measured in a modified Bruker-Axs D8 diffractometer with parallel beam optics and a PSD LynxEye silicon strip detector. This instrument uses an unmonochromated Cu Kα source operated at 40 kV with 30 mA emission current. The incident beam angle was set at 0.5° and the angular range of the patterns collected was 10° < 2θ < 65° with a step size of 0.05° counted at 1 s/step.

Scanning Electron Microscopy (SEM) was performed to determine surface morphology and film thickness using a JEOL JSM-6301F Field Emission SEM at an accelerating voltage of 5 keV.

Optical spectra were taken using a Perkin Elmer Fourier transform Lambda 950 spectrometer over a wavelength range of 190 nm to 2500 nm. This range encompasses the ultraviolet (UV), visible and near infrared (NIR) regions. The spectra were referenced against an air background.

X-ray photoelectron spectroscopy (XPS) was performed in a Thermo Scientific K-alpha photoelectron spectrometer using monochromatic Al-K$_\alpha$ radiation. Survey scans were collected in the range 0–1100 eV (binding energy) at a pass energy of 160 eV. Higher resolution scans were recorded for the main core lines at a pass energy of 20

eV. Valence band spectra were also recorded. Peak positions were calibrated to adventitious carbon (284.5 eV) and plotted using the CasaXPS software.

Density Functional Theory

Hybrid density functional theory (hDFT) calculations were implemented using the Vienna *ab initio* Simulation Package (VASP) in order to investigate the electronic structure of crystalline β-Ta_2O_5. Hybrid functionals have been proven to show increased accuracy and correlation with experimental results compared to standard DFT functionals, which tend to vastly underestimate the band gap.[36–41] Our calculations utilised the HSE06 (Heyd-Scuseria-Ernzerhoff)[42] screened hybrid functional alongside the PBE0 hybrid functional.[43,44] PBE0 is based on the PBE (Perdew Burke Ernzerhoff) functional but incorporates 25% exact Hartree-Fock exchange which, together with the 100% electron correlation and 75% PBE exchange allows for a modest correction of the "self-interaction-error" (SIE) in a system, whilst keeping reasonable computational expense. These have both been used in previous *ab-initio* calculations to describe β-Ta_2O_5.[11,45] Calculations using these functionals, however, have failed to describe the electronic and optical properties accurately and as such we also used the PBE functional with 30% exact HF exchange. In order to describe the interactions between the valence electrons and the core (Ta:[Xe] and O:[He]) electrons, the Projector Augmented Wave Method (PAW)[46] was employed.

A plane wave energy cut-off of 520eV was deemed sufficient for convergence alongside a Γ-centred k-point grid of 4x7x3 for the 14 atom cell (which belongs to the *Pccm* space group as shown in Figure 1). Initially, a structural optimisation was carried out on β-Ta_2O_5 relaxing the lattice vectors, cell angles, cell volume and atomic positions. Convergence was deemed to be complete when the forces on all the atoms were less than 0.01eV $Å^{-1}$. Following the structural optimisation, a density of states (DoS) calculation, band structure and optical absorption spectrum was calculated. The optical absorption spectrum and the optical transition matrix elements were calculated within the transversal approximation and PAW method.[47] In this approach the absorption spectrum is summed over all direct valence band to conduction band transitions ignoring indirect and intraband absorption.[48] For increased accuracy the Γ-centred k-point grid was increased to 5x8x4. This method has been shown to provide

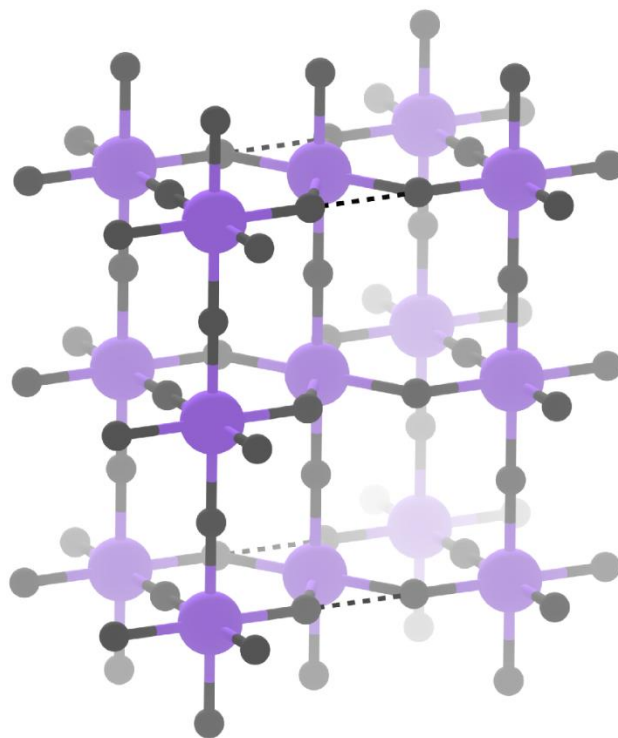sensible absorption spectra with regards to experiment, despite not addressing the electron-hole correlation.[49–56]

Figure 1: The unit cell of β-Ta₂O₅ (space group Pccm) where Ta = purple and O = dark grey. The unit cell boundaries are displayed as dashed lines.

Photocatalytic activity

The films were cleaned in propan-2-ol, oven dried and coated with a stearic acid (0.05 M solution in chloroform) layer *via* dip coating. The photocatalytic activity of the films was monitored by Fourier transform-infrared (FT-IR) spectroscopy using a PerkinElmer RX-I instrument. The IR spectrum of each acid-over layer was recorded over the range $3000 - 2700$ cm^{-1} and the areas of the peaks between 2950 and 2870 and 2870 and 2830 cm^{-1} integrated. These peaks respectively represent the C–H antisymmetric and symmetric stretches of stearic acid and can be directly related to the concentration of stearic acid on the film's surface.[57] The samples were irradiated using a 254 nm (4.9×10^{15} photon cm^{-2}s^{-1}) UV lamp. The IR spectrum of each acid-over layer was then recorded over the same range $3000–2700$ cm^{-1}. The peaks integrated in the same manner at each interval are proportional to the stearic acid present in units molecules cm^{-2}. Using a pre-determined conversion factor (9.7×10^{15}

6

molecules $\equiv$ 1 A.cm^{-1}, where A is absorption) allows a reaction rate to be expressed in units molecules degraded. cm^{-2}.s^{-1}.[57]

Photo-induced hydrophilicity (PIH)

Water droplet contact angles were measured using a First Ten angstroms 1000 device with a side mounted rapid fire camera fire casting 3 µL droplet from a fixed height onto the surface. Photoinduced hydrophilicity was examined by placing the samples under a UVC (254 nm) lamp for 12 hours then re-measuring the water contact angle.

Results and Discussion

Amorphous Ta_2O_5 films were grown on quartz *via* AACVD from a methanolic solution of $Ta(OEt)_5$ at 450 ºC. The deposition resulted in the complete coverage of the quartz substrate with a highly transparent thin film. A post heat treatment at 1000 ºC led to the formation of crystalline β - Ta_2O_5 films. The as deposited and post heat-treated films were well adhered to their quartz substrates, passing the Scotch^{TM} tape test, and were resistant to scratching using a stainless steel scaple.[58]

X-ray diffraction (XRD) of the as deposited film showed it to be amorphous (Figure 2). Annealing at 1000 ºC in air for 12 hours allowed it to crystallize into the low temperature phase with an orthorhombic unit cell (PDF no. 01-070-9177) as previously reported for both CVD and PVD grown films.[5,59,60] No occurrence of a secondary phase was observed. Preferred orientation was observed in the (200) and (202) planes from texture coefficient calculations. This has been previously reported for β-Ta_2O_5 films grown from $Ta(OEt)_5$ via metal organic solution deposition.[14] An estimate of the crystallite size was determined to be 40 nm by applying the Scherrer equation to the XRD data (see supporting information).
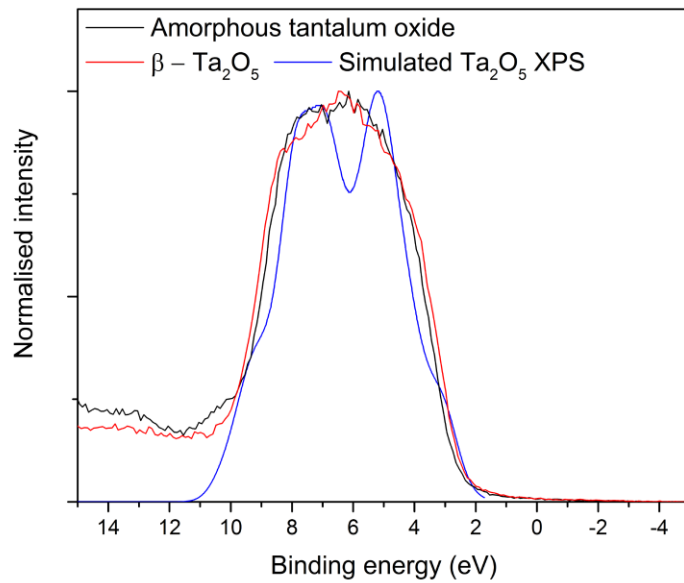
a)
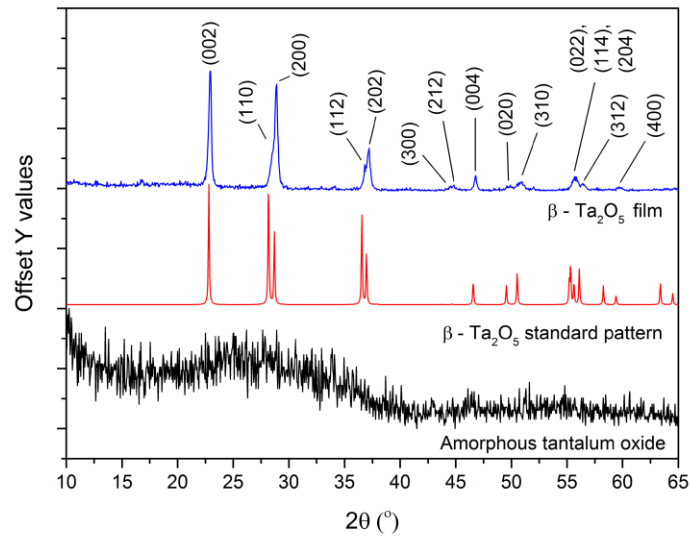
b)
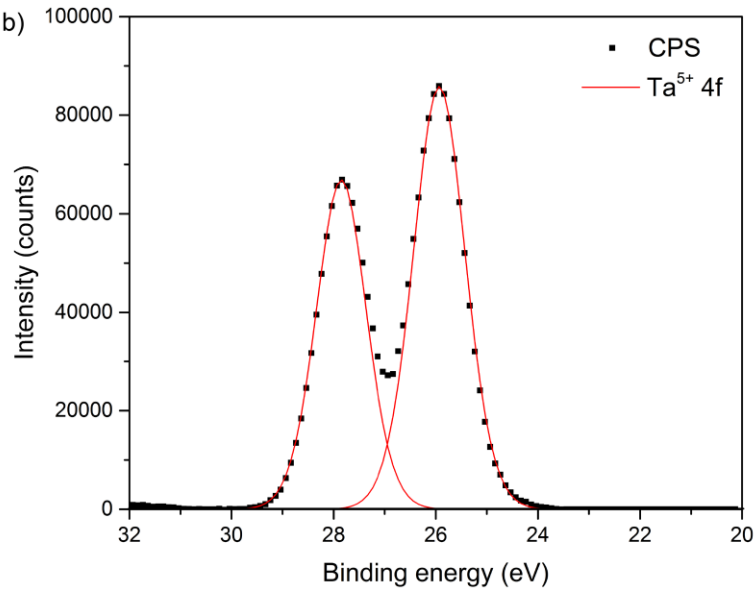
c)

Figure 2: a) The XRD patterns of the as deposited and annealed Ta₂O₅ film grown by an aerosol-assisted chemical vapour deposition (AACVD) method using a methanol/Ta(OEt)₅ solution. The standard pattern for β-Ta₂O₅ also shown for comparison. b) The core level XPS spectra of the Ta 4f transitions for the as grown amorphous Ta₂O₅ films, where solely Ta⁵⁺ was observed at the surface. c) The valence band structure of both the amorphous and crystalline films measured by XPS at low energy along with the simulated valence band.

X-ray photoelectron spectroscopy (XPS) was carried out to determine the surface composition and oxidation state of the amorphous and the crystallized film. Figure 2b shows the Ta 4f transition for the amorphous film consisting of a doublet separated by 1.9 eV. The $4f_{5/2}$ peak appears at 25.9 eV corresponding to Ta^{5+} as expected.[61,62] For the β-Ta₂O₅ sample, the peak is shifted by 0.3 eV to 25.6 eV (see supporting information). Neither film shows any presence of a reduced Ta state. Valence band XPS of both the amorphous and crystalline films is shown in Figure 2c along with the simulated spectrum as determined by DFT. The calculated density of states (DoS) was weighted using the atomic orbital photoionisation cross-sections formulated by Yeh and Lindau[63] simulating a valence band XPS that can be compared directly with experiment, carried out with a 0.47 eV Gaussian smearing to match experimental broadening. This method has been successfully applied in previous work to deliver accurate insights into the states that contribute to the XPS data.[64–67]

The spectra for amorphous and crystalline β-Ta₂O₅ are almost identical and dominated by a broad feature mainly associated with O 2p states. The width of the experimental and simulated valence bands are very similar although the simulated spectrum has some fine structure, consisting of a trough at ~6 eV which is due to a reduction in density of states at ~6 eV in the band structure. The valence band onset of the experimental data, determined through simple linear extrapolation, was observed at ca. 2.5 eV. As our XPS was measured relative to the Fermi level of Ta₂O₅, this showed that the Fermi level was approximately 1.5 eV below the conduction band as our measured band gap, typical of Ta₂O₅, was 4.0 eV.

Scanning electron microscopy (SEM) images shown in Figure 3 detail the change in morphology upon annealing from the amorphous to crystalline state. The as deposited film (Film 3a) was essentially featureless with a morphology consisting of dome like structures a few 100 nm in diameter. Some regions show extended pinholes, possibly arising from the rapid removal of organic impurities during the deposition process. Upon annealing, the film becomes denser, as indicated by the change in film thickness from 320 (amorphous) and 260 nm (β-Ta₂O₅). Furthermore, there appears to be grain

growth (Figure 3b), as a result of joining the domes-like structures to produce larger, more structured features. This is typical of a high temperature annealing step due to the increase in surface mobility during the amorphous to crystalline phase transformation. This allows the film to reduce total energy by reducing boundaries through the formation of larger grains/crystallites.[14] The relatively flat and textureless appearance of both films is ideal for optoelectronic applications as it prevents light scattering and maintains transparency across the visible and near IR spectrum. This was indeed the case when the optical properties of the amorphous and the crystalline films were analysed using UV-Vis spectroscopy (Figure 3c). Both films were highly transparent across the spectrum measured - generally with transmittance above 80%. The reflectance of the films was below 20% at wavelengths above 500 nm. Between 500 nm to 200 nm the reflectance values steadily rise to 40%.
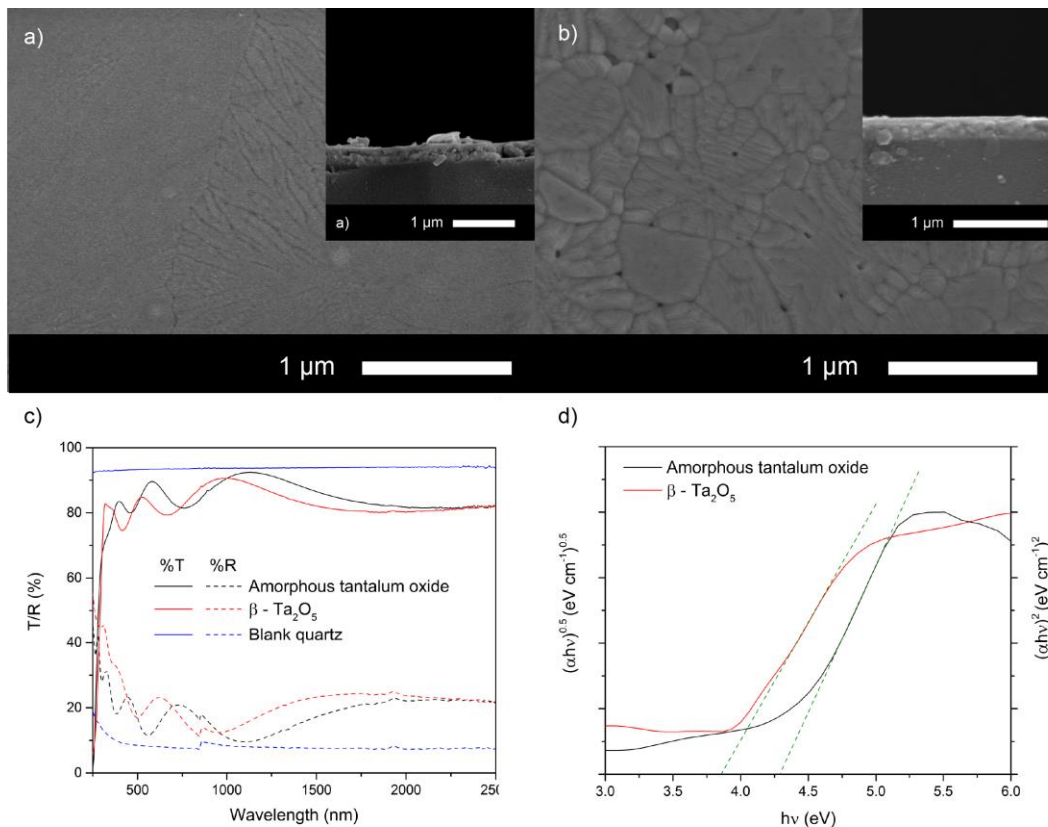

Figure 3: SEM images showing the a) as deposited and b) annealed Ta₂O₅ films on quartz substrates with the corresponding cross-sectional images shown inset. Films were grown by aerosol-assisted chemical vapour deposition (AACVD) using methanol/Ta(OEt)₅ at 450 ºC and annealed in air at 1000 ºC. c) UV – Vis spectra of quartz (blue), amorphous (black) and crystalline (red) Ta₂O₅ on quartz. d) The optical indirect (amorphous) and direct (β) band gaps calculated using the Tauc plot.

The refractive indices (n) of the films were calculated using the Swanepoel method from interference fringes observed in transmission (Table 1). Both films showed values of 1.7 and 1.8 at 460 nm and 520 nm, respectively. The refractive index is highly dependent on the crystallinity and impurity/defect concentration of the films. Therefore the observed increase in n for the annealed film can be attributed to the increase in crystallinity and decrease in defects. These values lie within the range reported in literature for amorphous and crystalline β-Ta_2O_5.[18,68]

Table 1: The band gap and refractive index at various wavelengths for the as deposited and annealed tantalum oxide films on quartz.

Film	Band gap / eV	Refractive index (wavelength / nm)
Amorphous tantalum oxide	4.3 (ind)	1.7 (460)
β-Ta_2O_5	3.8 (dir)	1.8 (520)

The optical band gap of Ta_2O_5 in both the amorphous and orthorhombic polymorphs is known to vary, with a strong influence on fabrication method. Much like silicon, the band gap reduces post crystallization. It is also known that the band gap converts from indirect to direct upon crystalisation to β-Ta_2O_5. Here, the optical band gap (calculated using the Tauc plot, Figure 3d) for the amorphous and crystalline films was 4.3 and 3.8 eV respectively, both lying within the range that is typically reported for Ta_2O_5 films. Furthermore, unlike computational simulations carried out in literature to date, which underestimate the optical band gap of β-Ta_2O_5, our calculations match well with the experimental value.

Previous *ab-initio* work on β-Ta_2O_5 have involved the use of various DFT functionals (Local Density Approximation (LDA), Generalised Gradient Approximation (GGA) and GGA+U^d+U^p (where +U^x refers to a Hubbard-like "U" parameter which introduces a penalty for partial occupation at a site, in this case U^d and U^p refer to corrections applied to the Ta d orbitals and the O p orbitals)[11,56,69–71], hybrid DFT functionals (HSE06, B3LYP (Becke-Lee-Yang-Parr)[72] and PBE0)[11,45] and the GW (Green's function) approximation.[70] The calculated band gaps from these studies are displayed in Table 2 and show results that are vastly underestimated in comparison to

the experimental measured optical band gap from this study (~3.8 eV) and previous experimental reports. The LDA and GGA bandgaps are ~3.6 eV below the optical band gap,[11,56,69] whilst the HSE06 and PBE0 values produced by Wu *et al.*[11] and Nashed *et al.*[45] respectively, which although are an improvement on the LDA and GGA are still underestimated by >1.35 eV. Our calculations on the fundamental band gap of β-Ta_2O_5 using HSE06 and PBE0 confirm the difference between the fundamental band gap and the optical band gap. The calculated PBE0 band gap reported here is ~2.25 eV differing by 0.2 eV to that reported by Nashad *et al*. However, this could be due to the relatively low plane wave energy cut-off and the small Monkhorst-Pack k-point grid employed in their calculations.[45] Our HSE06 calculation on the other hand provides a fundamental band gap of ~1.4 eV which is around 0.5 eV different to that calculated by Wu *et al.*, which could be explained by the authors lack of structural optimisation with HSE06.[11]

To understand the differences between the fundamental band gaps from the calculations and the optical band gaps seen in experiment, we have calculated the optical absorption spectrum. The HSE06 and PBE0 calculated optical band gaps (E_g^{opt}) are ~2.64 eV and ~3.37 eV respectively which shows that the direct allowed transition from the valence band to the conduction band is much larger than the direct fundamental band gap (VBM to CBM) (~1.4 eV and ~2.25 eV respectively). Clearly the PBE0 optical band gap is closer to experiment than the HSE06 value yet is still ~0.43 eV less than the experimental optical band gap of 3.8 eV.

Table 2: Tabulated direct (E_g^{dir}) and optical (E_g^{opt}) band gaps calculated using various DFT functionals for β-Ta_2O_5 from the literature alongside results from this work. PBE with 30% HF exchange provides an accurate description of the optical band gap in close agreement with experiment. Band gaps calculated in this work are displayed in italics and/or in brackets.

	LDA [69]	GGA[11,56,69]	GGA+U^d+U^p[71]	HSE06[11]	PBE0 [11]	B3LYP [11]	GW [70]	PBE (30% HF exchange)
E_g^{dir} (eV)	0.2	0.1-0.2	2.24	0.9 *(1.4)*	2.45 *(2.25)*	2.15	1.03	*2.57*
E_g^{opi}	--	--	--	*(2.64)*	*(3.37)*	--	--	*3.83*

12

We have demonstrated that PBE with 30% HF exchange gives the correct optical band gap for β-Ta_2O_5 (~3.83 eV) with a fundamental band gap of 2.57 eV. The band structure is displayed in Figure 4 and shows the valence band maximum (VBM) at the X high symmetry point making this material a direct band gap material. However, the difference in energy between the X and S points is ~2 x 10^{-4} eV making X and S virtually indistinguishable from each other, as shown by the horizontal band from X-S. The effective hole masses at the VBM are 0.9 m_e, 1.28 m_e and 38.8 m_e from X-U, X-Γ and X-S respectively, indicating that any holes produced will be quite heavy and thus are expected to possess low mobility. The conduction band minimum appears at X and displays favourable dispersion in the X-U direction with an effective electron mass of 0.23 m_e comparable to the wide band gap material In_2O_3 (~0.22 m_e[73]) but heavier electron masses of 0.93 m_e and 35.70 m_e in the X-Γ and X-S directions respectively.
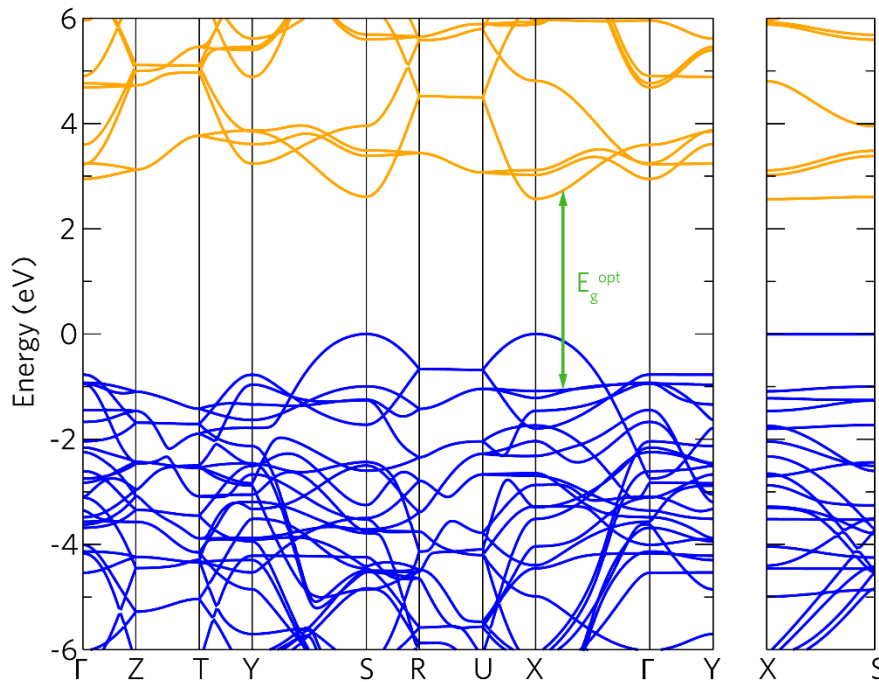

Figure 4: The calculated band structure for β-Ta_2O_5 using the PBE functional with 30% HF exchange. The blue bands represent the valence band with the VBM set to 0 eV and the orange bands represent the conduction bands. The strong optical absorption is displayed with the green arrow marking the transition from ~1 eV below the VBM between X-Gamma to the bottom conduction band. The band structure from X-S is also shown.

Figure 5 shows the calculated absorption spectrum of β-Ta$_2$O$_5$, where there is a small absorption onset at ~3.28 eV and a strong absorption at ~3.83 eV, also observed by experiment. The strong absorption starts from a band ~1 eV below the VBM to the bottom conduction band ~0.5 eV above the CBM at a point between the X and Γ high symmetry points.
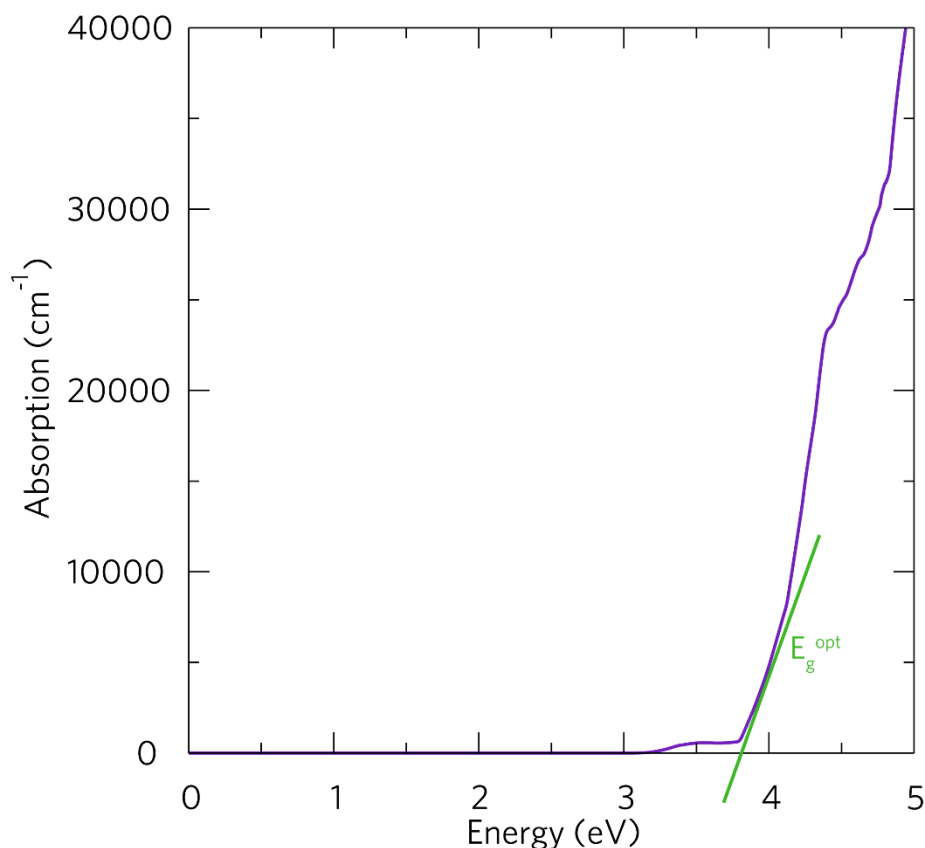

Figure 5: The calculated optical absorption spectrum for β-Ta$_2$O$_5$ summed over all possible direct valence to conduction band transitions. This spectrum is calculated using the PBE functional with 30% HF exchange. The strong optical absorption is labelled with the green line and the intersection with the x axis corresponds to E$_g$^{opt}.

Functional properties

The photocatalytic activity of both amorphous and β-Ta$_2$O$_5$ films was examined using 254 nm (4.9 x 10^{15} photon cm^{-2}s^{-1}) irradiation for their ability to photomineralise stearic acid – a model organic pollutant with a low vapour pressure (Figure 6a and 6b).[74] A control sample, consisting of a glass slide coated with stearic acid was also tested to account for any loss of stearic acid due to evaporation or photodegradation (See supporting information).

The amorphous Ta_2O_5 sample showed a stearic acid destruction rate of 2.73 x 10^{11} molecules.cm^{-2}.s^{-1} (FQE = 5.52 x 10^{-5} molecules per incident photon). This was almost an order of magnitude greater than what was observed for crystalline β-Ta_2O_5, which showed a stearic acid destruction rate of 6.98 x 10^{10} molecules.cm^{-2}.s^{-1} (FQE = 1.41 x 10^{-5} molecules per incident photon). This is surprising, as metal oxides often show a higher photoactivity when crystalline (as opposed to amorphous) due to superior charge carrier mobility from the bulk to the surface where photocatalysis takes place.[75] Here, the fact that the amorphous material was more active may be due to a number of reasons. For instance, 254 nm light does not penetrate deep into the material (Figure 4c), meaning most charge carriers are formed at the material surface. The penetration depth (δp/ nm) can be determined from the following equation:

$$\delta_p = 1/\alpha \qquad \text{Eq. 1}$$

Where the absorption coefficient (α/ cm-1) can be determined using Eq.2 since we know the thickness of the films (z) and their transmittance (I/I_0) from the UV-visible absorption behavior.

$$I/I_0 = e^{-\alpha z} \qquad \text{Eq. 2}$$

The penetration depth is the distance that light can travel before it reaches 1/e of its surface value (i.e. the distance in which 63 % of light has been absorbed). In the case of our Ta_2O_5- films, the penetration depth at 254 nm was approximately 100 nm. In n-type metal oxides, the hole diffusion length is typically far shorter than the electron diffusion length. For instance, in TiO_2, the hole diffusion length is roughly 10 nm long[76] whereas the electron diffusion length is several micrometers.[77] The hole diffusion length differs in various n-type metal oxides, ranging from ~ 4 nm in α-Fe_2O_3[78], to ~ 75 nm in $BiVO_4$[79] and ~ 150 nm in WO_3[80]. We suspect that the hole diffusion length in amorphous and crystalline Ta_2O_5 films would be of a similar order, therefore, we envisage that holes generated within the penetration depth (100 nm deep using 254 nm light) can diffuse to the material surface and react efficiently even in the amorphous material. This means that a higher charge carrier mobility, often associated with more crystalline material, becomes less of a factor as photo-generated charges do not need to travel far to reach the surface. Less crystalline materials are more defective, where these defects may assist in the trapping and separation of photo-generated charge, thereby minimizing charge carrier recombination. Also, the

15

wider band gap found in amorphous films may result in the generation of charge carriers with a greater potential energy to photocatalyse stearic acid. Takahara *et al.* also found that amorphous Ta_2O_5 showed a higher photocatalytic activity for overall water splitting compared to a crystalline sample.[7]
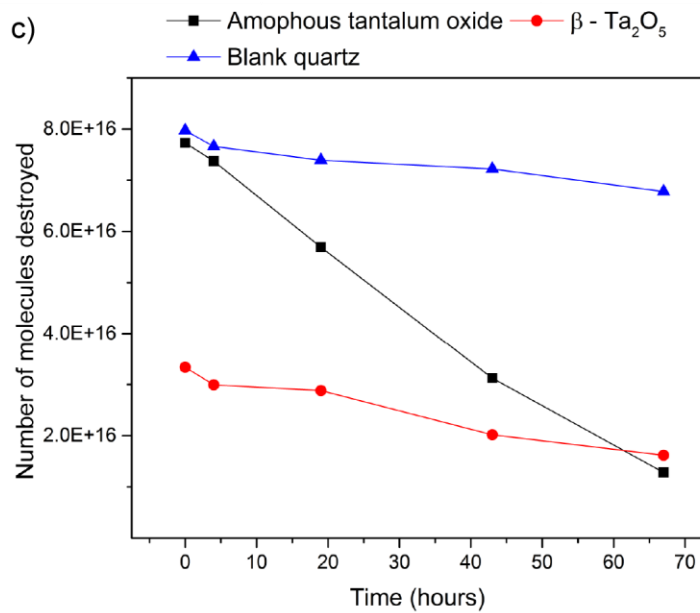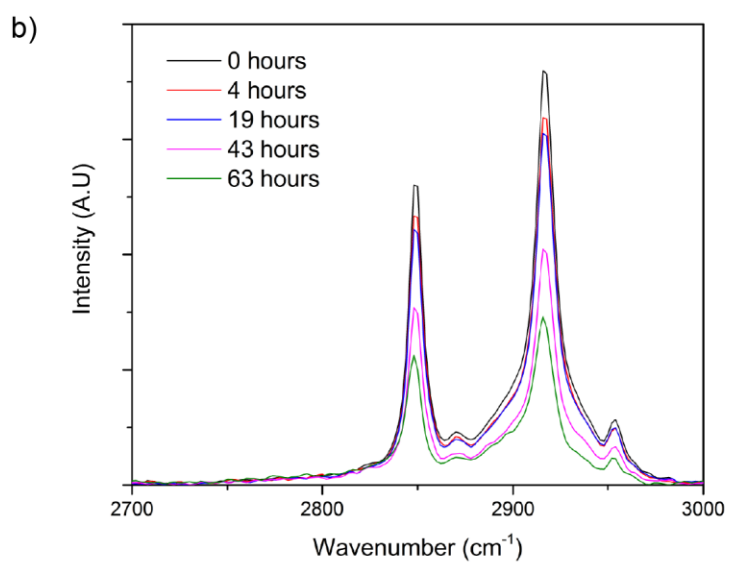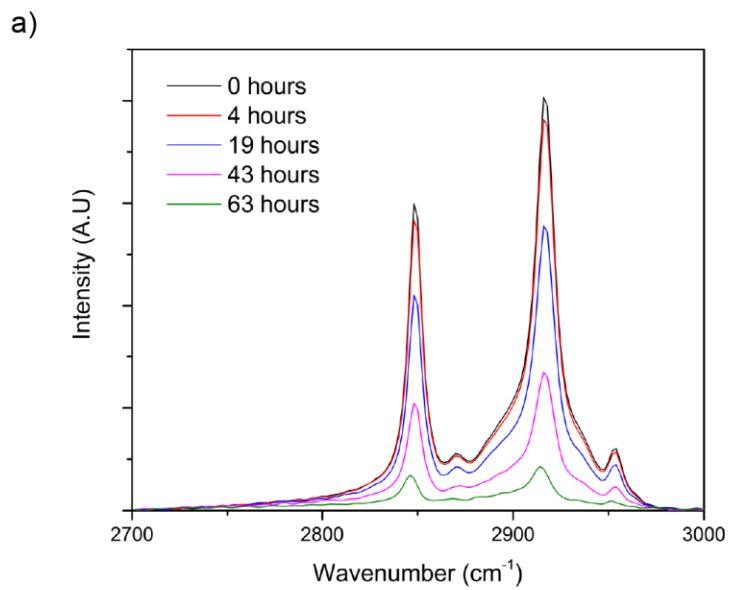
a)

b)

c)

Figure 6: The change in absorption of the C–H antisymmetric and symmetric stretches of stearic acid with irradiation time for a) the amorphous and b) the crystalline β-Ta₂O₅ films. c) The number of stearic acid molecules destroyed on the amorphous, crystalline and blank quartz samples with irradiation time.

Water contact angle measurements were measured before and after irradiation on both amorphous and crystalline β-Ta$_2$O$_5$ films to determine whether their surface becomes hydrophilic upon irradiation, much like TiO$_2$ (Figure 7) (see supporting information for measurements carried out on pre and post irradiated blank quartz substrate). The photon energy (~4.9 eV) from a 254 nm (4.9 x 10^{15} photon cm^{-2}s^{-1}) lamp was sufficiently high enough to activate the band gaps of both films and therefore used to induce any photoinduced hydrophilicity. The amorphous film showed a slight increase in hydrophilicity with a decrease in the water contact angle from 70° to 40°. For the crystalline sample, no change in the contact angle (25°) was observed upon irradiation. Interestingly this has been seen previously for PVD deposited films, where Gonzale-Elipe *et. al.* found that amorphous Ta$_2$O$_5$ showed more pronounced photo-induced hydrophilicity than an annealed sample.[81]
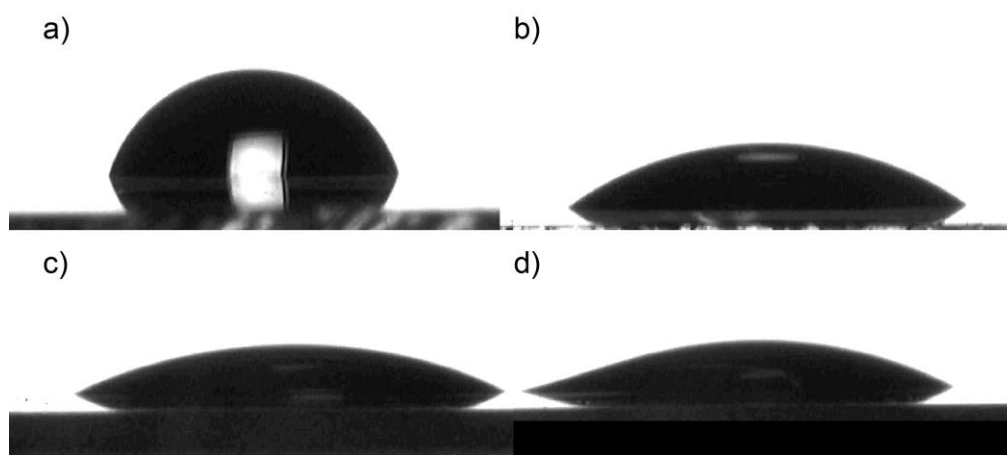

Figure 7: The water contact angle measurements for a,b) amorphous and c,d) crystalline Ta₂O₅ a, c) before and b,d) after irradiation for 12 hours using a 254 nm lamp.

Conclusion

An amorphous Ta$_2$O$_5$ film was successfully grown on quartz substrates for the first time *via* the aerosol-asssisted chemical vapour deposition (AACVD) reaction of Ta(OEt)$_5$ in methanol at 450 ^{o}C. An annealing step was performed to obtain the orthorhombic crystallographic phase and the effects on the structural and optical properties of the films were investigated by both computation and experiment. SEM

analysis showed the films to be relatively flat with a slight increase in structure due to grain grown as a result of the thermal treatment. This resulted in an increase in hydrophilicity, with a reduction in the water contact angle from 70° to 40°. The transformation from the amorphous to the crystalline phase of the Ta_2O_5 caused a decrease in the optical band gap from 4.3 to 3.8 eV. The experimental optical band gap for β-Ta_2O_5 closely matched the band gap determined by hybrid density functional theory (3.83 eV). Interestingly, amorphous Ta_2O_5 was substantially more photocatalytically active in the decomposition of stearic acid under 254 nm light.

Supporting information

Particle size calculations using the Scherrer equation

Core level Ta 4f XPS spectrum for β-Ta_2O_5 film

Stearic acid test results for blank quartz control.

Acknowledgment

References

(1)   Murawala, P. A.; Sawai, M.; Tatsuta, T.; Tsuji, O.; Fujita, S.; Fujita, S. Structural and Electrical Properties of Ta2O5 Grown by the Plasma-Enhanced Liquid Source CVD Using Penta Ethoxy Tantalum Source. *Jpn. J. Appl. Phys.* **1993**, *32* (1S), 368.

(2)   Matsui, Y.; Hiratani, M.; Kimura, S.; Asano, I. Combining Ta2O5 and Nb2O5 in Bilayered Structures and Solid Solutions for Use in MIM Capacitors. *J. Electrochem. Soc.* **2005**, *152* (5), F54–F59.

(3)   Devine, R. A. B.; Autran, J. L.; Paillet, P.; Leray, J. L. Electrical Properties of Ta2O5 Films Obtained by Plasma Enhanced Chemical Vapor Deposition Using a TaF5 Source. *Appl. Phys. Lett.* **1996**, *86* (13), 1775–1777.

(4)   Robertson, J. High Dielectric Constant Gate Oxides for Metal Oxide Si

Transistors. *Reports Prog. Phys.* **2005**, *69* (2), 327–396.

(5)   Lee, J. S.; Chang, S. J.; Chen, J. F.; Sun, S. C.; Liu, C. H.; Liaw, U. H. Effects of O2 Thermal Annealing on the Properties of CVD Ta2O5 Thin Films. *Mater. Chem. Phys.* **2003**, *77* (1), 242–247.

(6)   Suzuki, T. M.; Nakamura, T.; Saeki, S.; Matsuoka, Y.; Tanaka, H.; Yano, K.; Kajino, T.; Morikawa, T. Visible Light-Sensitive Mesoporous N-Doped Ta2O5 Spheres: Synthesis and Photocatalytic Activity for Hydrogen Evolution and CO2 Reduction. *J. Mater. Chem.* **2012**, 24584–24590.

(7)   Takahara, Y.; Kondo, J. N.; Takata, T.; Lu, D.; Domen, K. Photocatalytic Activity for the Overall Water Decomposition. *Chem. Mater.* **2001**, *13* (4), 1194–1199.

(8)   Gonçalves, R. V; Migowski, P.; Wender, H.; Eberhardt, D.; Weibel, D. E.; Sonaglio, F. C.; Zapata, M. J. M.; Dupont, J.; Feil, A. F.; Teixeira, S. R. Ta2O5 Nanotubes Obtained by Anodization: Effect of Thermal Treatment on the Photocatalytic Activity for Hydrogen Production. *J. Phys. Chem. C* **2012**, *116* (26), 14022–14030.

(9)   Morikawa, T.; Saeki, S.; Suzuki, T.; Kajino, T.; Motohiro, T. Dual Functional Modification by N Doping of Ta[sub 2]O[sub 5]: P-Type Conduction in Visible-Light-Activated N-Doped Ta[sub 2]O[sub 5]. *Appl. Phys. Lett.* **2010**, *96* (14), 142111.

(10)   Sato, S.; Morikawa, T.; Saeki, S.; Kajino, T.; Motohiro, T. Visible-Light-Induced Selective CO2 Reduction Utilizing a Ruthenium Complex Electrocatalyst Linked to a P-Type Nitrogen-Doped Ta 2O5 Semiconductor. *Angew. Chemie - Int. Ed.* **2010**, *49* (30), 5101–5105.

(11)   Wu, Y.-N.; Li, L.; Cheng, H.-P. First-Principles Studies of Ta 2 O 5 Polymorphs. *Phys. Rev. B* **2011**, *83*.

(12)   Zhou, Y. L.; Niinomi, M.; Akahori, T.; Fukui, H.; Toda, H. Corrosion Resistance and Biocompatibility of Ti-Ta Alloys for Biomedical Applications. *Mater. Sci. Eng. A* **2005**, *398* (1–2), 28–36.

(13)   Nakagawa, Y.; Okada, T. Material Constants of New Piezoelectric Ta2O5 Thin Films. *J. Appl. Phys.* **1990**, *68* (2), 556–559.

(14)   Joshi, P. C.; Cole, M. W. Influence of Postdeposition Annealing on the Enhanced Structural and Electrical Properties of Amorphous and Crystalline Ta2O5 Thin Films for Dynamic Random Access Memory Applications. *J. Appl. Phys.* **1999**, *86* (2), 871–880.

(15)   Lehovec, K. Lattice Structure of β-Ta2O5. *J. Less Common Met.* **1964**, *7* (6), 397–410.

(16)   Askeljung, C.; Marinder, B.-O.; Sundberg, M. Effect of Heat Treatment on the Structure of L-Ta 2 O 5:: A Study by XRPD and HRTEM Methods. *J. Solid State Chem.* **2003**, *176* (1), 250–258.

(17)   Hiratani, M.; Kimura, S.; Hamada, T.; Iijima, S.; Nakanishi, N. Hexagonal

Polymorph of Tantalum-Pentoxide with Enhanced Dielectric Constant. *Appl. Phys. Lett.* **2002**, *81*, 2433.

(18)   Oehrlein, G. S.; d'Heurle, F. M.; Reisman, A. Some Properties of Crystallized Tantalum Pentoxide Thin Films on Silicon. *J. Appl. Phys.* **1984**, *55* (10), 3715–3725.

(19)   Ivanov, M. V.; Perevalov, T. V.; Aliev, V. S.; Gritsenko, V. A.; Kaichev, V. V. Electronic Structure of ??-Ta2O5 with Oxygen Vacancy: Ab Initio Calculations and Comparison with Experiment. *J. Appl. Phys.* **2011**, *110* (2).

(20)   Liu, X. Q.; Han, X. D.; Zhang, Z.; Ji, L. F.; Jiang, Y. J. The Crystal Structure of High Temperature Phase Ta 2 O 5. *Acta Mater.* **2007**, *55* (7), 2385–2396.

(21)   Miyazaki, S. Photoemission Study of Energy-Band Alignments and Gap-State Density Distributions for High-K Gate Dielectrics. *J. Vac. Sci. Technol. B* **2001**, *19* (6), 2212–2216.

(22)   Hashimoto, C.; Oikawa, H.; Honma, N. Leakage-Current Reduction in Thin Ta 2 O 5 Films for High-Density VLSI Memories. *IEEE Trans. Electron Devices* **1989**, *36* (1), 14–18.

(23)   Seki, S.; Unagami, T.; Kogure, O.; Tsujiyama, B. Formation of High- quality, Magnetron- sputtered Ta2O5 Films by Controlling the Transition Region at the Ta2O5/Si Interface. *J. Vac. Sci. Technol. A* **1987**, *5* (4), 1771–1774.

(24)   Chiu, F.-C.; Wang, J.-J.; Lee, J. Y.; Wu, S. C. Leakage Currents in Amorphous Ta2O5 Thin Films. *J. Appl. Phys.* **1997**, *81* (10), 6911–6915.

(25)   Forsgren, K.; Anders, H. Halide Chemical Vapour Deposition of Ta 2 O 5. *Thin Solid Films* **1999**, *343*, 111–114.

(26)   Siodmiak, M.; Frenking, G.; Korkin, A. Initial Reactions in Chemical Vapor Deposition of Ta2O5 from TaCl5 and H2O. An Ab Initio Study. *J. Phys. Chem. A* **2000**, *104* (6), 1186–1195.

(27)   Knapp, C. E.; Carmalt, C. J. Solution Based CVD of Main Group Materials. *Chem. Soc. Rev.* **2016**, *45* (4), 1036–1064.

(28)   Bawaked, S. M.; Sathasivam, S.; Bhachu, D. S.; Chadwick, N.; Obaid, A. Y.; Al-Thabaiti, S.; Basahel, S. N.; Carmalt, C. J.; Parkin, I. P. Aerosol Assisted Chemical Vapor Deposition of Conductive and Photocatalytically Active Tantalum Doped Titanium Dioxide Films. *J. Mater. Chem. A* **2014**, *2* (32), 12849–12856.

(29)   Chadwick, N.; Sathasivam, S.; Kafizas, A.; Bawaked, S. M.; Obaid, A. Y.; Al-Thabaiti, S.; Basahel, S. N.; Parkin, I. P.; Carmalt, C. J. Combinatorial Aerosol Assisted Chemical Vapour Deposition of a Photocatalytic Mixed SnO 2/TiO 2 Thin Film. *J. Mater. Chem. A* **2014**, *2* (14), 5108–5116.

(30)   Sathasivam, S.; Bhachu, D. S.; Lu, Y.; Chadwick, N.; Althabaiti, S. A.; Alyoubi, A. O.; Basahel, S. N.; Carmalt, C. J.; Parkin, I. P. Tungsten Doped TiO2 with Enhanced Photocatalytic and Optoelectrical Properties via Aerosol Assisted Chemical Vapor Deposition. *Sci. Rep.* **2015**, *5*.

(31)   Sathasivam, S.; Arnepalli, R. R.; Kumar, B.; Singh, K. K.; Visser, R. J.; Blackman, C. S.; Carmalt, C. J. Solution Processing of GaAs Thin Films for Photovoltaic Applications. *Chem. Mater.* **2014**, *26* (15), 4419–4424.

(32)   Sathasivam, S.; Arnepalli, R. R.; Singh, K. K.; Visser, R. J.; Blackman, C. S.; Carmalt, C. J. A Solution Based Route to GaAs Thin Films from As (NMe 2) 3 and GaMe 3 for Solar Cells. *RSC Adv.* **2015**, *5* (16), 11812–11817.

(33)   Ponja, S. D.; Sathasivam, S.; Parkin, I. P.; Carmalt, C. J. Transparent Conductive Aluminium and Fluorine Co-Doped Zinc Oxide Films via Aerosol Assisted Chemical Vapour Deposition. *RSC Adv.* **2014**, *4* (91), 49723–49728.

(34)   Bhachu, D. S.; Sathasivam, S.; Carmalt, C. J.; Parkin, I. P. PbO-Modified TiO2 Thin Films: A Route to Visible Light Photocatalysts. *Langmuir* **2014**, *30* (2), 624–630.

(35)   Sathasivam, S.; Bhachu, D. S.; Lu, Y.; Bawaked, S. M.; Obaid, A. Y.; Al- Thabaiti, S.; Basahel, S. N.; Carmalt, C. J.; Parkin, I. P. Highly Photocatalytically Active Iron (III) Titanium Oxide Thin Films via Aerosol- Assisted CVD. *Chem. Vap. Depos.* **2015**, *21* (1-2–3), 21–25.

(36)   Burbano, M.; Scanlon, D. O.; Watson, G. W. Sources of Conductivity and Doping Limits in CdO from Hybrid Density Functional Theory. *J. Am. Chem. Soc.* **2011**, *133* (38), 15065–15072.

(37)   Rajpalke, M. K.; Linhart, W. M.; Birkett, M.; Yu, K. M.; Scanlon, D. O.; Buckeridge, J.; Jones, T. S.; Ashwin, M. J.; Veal, T. D. Growth and Properties of GaSbBi Alloys Growth and Properties of GaSbBi Alloys. **2014**, *142106* (2013), 0–4.

(38)   Zhang, S. B.; Northrup, J. E. Chemical Potential Dependence of Defect Formation Energies in GaAs: Application to Ga Self-Diffusion. *Phys. Rev. Lett.* **1991**, *67* (17), 2339.

(39)   Ganose, A. M.; Savory, C. N.; Scanlon, D. O. (CH3NH3) 2Pb (SCN) 2I2: A More Stable Structural Motif for Hybrid Halide Photovoltaics? *J. Phys. Chem. Lett.* **2015**, *6* (22), 4594–4598.

(40)   Walsh, A.; Chen, S.; Wei, S. H.; Gong, X. G. Kesterite Thin-Film Solar Cells: Advances in Materials Modelling of Cu 2 ZnSnS 4. *Adv. Energy Mater.* **2012**, *2* (4), 400–409.

(41)   Kehoe, A. B.; Temple, D. J.; Watson, G. W.; Scanlon, D. O. Cu 3 MCh 3 (M= Sb, Bi; Ch= S, Se) as Candidate Solar Cell Absorbers: Insights from Theory. *Phys. Chem. Chem. Phys.* **2013**, *15* (37), 15477–15484.

(42)   Paier, J.; Marsman, M.; Hummer, K.; Kresse, G.; Gerber, I. C.; Ángyán, J. G. Screened Hybrid Density Functionals Applied to Solids. *J. Chem. Phys.* **2006**, *124* (15), 154709.

(43)   Adamo, C.; Barone, V. Toward Reliable Density Functional Methods without Adjustable Parameters: The PBE0 Model. *J. Chem. Phys.* **1999**, *110* (13), 6158–6170.

(44)   Paier, J.; Hirschl, R.; Marsman, M.; Kresse, G. The Perdew–Burke–Ernzerhof Exchange-Correlation Functional Applied to the G2-1 Test Set Using a Plane-Wave Basis Set. *J. Chem. Phys.* **2005**, *122* (23), 234102.

(45)   Nashed, R.; Hassan, W. M. I.; Ismail, Y.; Allam, N. K. Unravelling the Interplay of Crystal Structure and Electronic Band Structure of Tantalum Oxide (Ta 2 O 5). *Phys. Chem. Chem. Phys.* **2013**, *15* (5), 1352–1357.

(46)   Blöchl, P. E. Projector Augmented-Wave Method. *Phys. Rev. B* **1994**, *50* (24), 17953.

(47)   Gajdoš, M.; Hummer, K.; Kresse, G.; Furthmüller, J.; Bechstedt, F. Linear Optical Properties in the Projector-Augmented Wave Methodology. *Phys. Rev. B* **2006**, *73* (4), 45112.

(48)   Adolph, B.; Furthmüller, J.; Bechstedt, F. Optical Properties of Semiconductors Using Projector-Augmented Waves. *Phys. Rev. B* **2001**, *63* (12), 125108.

(49)   Nie, X.; Wei, S.-H.; Zhang, S. B. Bipolar Doping and Band-Gap Anomalies in Delafossite Transparent Conductive Oxides. *Phys. Rev. Lett.* **2002**, *88* (6), 66405.

(50)   Walsh, A.; Da Silva, J. L. F.; Yan, Y.; Al-Jassim, M. M.; Wei, S.-H. Origin of Electronic and Optical Trends in Ternary In2O3(ZnO)(n) Transparent Conducting Oxides (n=1,3,5): Hybrid Density Functional Theory Calculations. *Phys. Rev. B* **2009**, *79* (7), 73105.

(51)   Scanlon, D. O.; Watson, G. W. (Cu2S2)(Sr3Sc2O5)− A Layered, Direct Band Gap, P-Type Transparent Conducting Oxychalcogenide: A Theoretical Analysis. *Chem. Mater.* **2009**, *21* (22), 5435–5442.

(52)   Walsh, A.; Yan, Y.; Huda, M. N.; Al-Jassim, M. M.; Wei, S.-H. Band Edge Electronic Structure of BiVO4: Elucidating the Role of the Bi S and V D Orbitals. *Chem. Mater.* **2009**, *21* (3), 547–551.

(53)   Allen, J. P.; Scanlon, D. O.; Piper, L. F. J.; Watson, G. W. Understanding the Defect Chemistry of Tin Monoxide. *J. Mater. Chem. C* **2013**, *1* (48), 8194–8208.

(54)   Allen, J. P.; Scanlon, D. O.; Watson, G. W. Electronic Structures of Silver Oxides. *Phys. Rev. B* **2011**, *84* (11), 115141.

(55)   Godinho, K. G.; Carey, J. J.; Morgan, B. J.; Scanlon, D. O.; Watson, G. W. Understanding Conductivity in SrCu 2 O 2 : Stability, Geometry and Electronic Structure of Intrinsic Defects from First Principles. *J. Mater. Chem.* **2010**, *20* (6), 1086–1096.

(56)   Gu, T.; Wang, Z.; Tada, T.; Watanabe, S. First-Principles Simulations on Bulk Ta2O5 and Cu/Ta2O5/Pt Heterojunction: Electronic Structures and Transport Properties. *J. Appl. Phys.* **2009**, *106* (10), 3713.

(57)   Mills, A.; McFarlane, M. Current and Possible Future Methods of Assessing the Activities of Photocatalyst Films. *Catal. Today* **2007**, *129* (1), 22–28.

(58)   Mittal, K. L. Adhesion Measurement of Thin Films. *Electrocompon. Sci. Technol.* **1976**, *3* (1), 21–42.

(59)   Aleshina, L. A.; Loginova, S. V. Rietveld Analysis of X-Ray Diffraction Pattern from β-Ta2O5 Oxide. *Crystallogr. Reports* **2002**, *47* (3), 415–419.

(60)   Pignolet, A.; Rao, G. M.; Krupanidhi, S. B. Rapid Thermal Processed Thin Films of Reactively Sputtered Ta 2 O 5. *Thin Solid Films* **1995**, *258* (1), 230–235.

(61)   Atanassova, E.; Tyuliev, G.; Paskaleva, A.; Spassov, D.; Kostov, K. XPS Study of N 2 Annealing Effect on Thermal Ta 2 O 5 Layers on Si. *Appl. Surf. Sci.* **2004**, *225* (1), 86–99.

(62)   Ho, S.-F.; Contarini, S.; Rabalais, J. W. Ion-Beam-Induced Chemical Changes in the Oxyanions (Moyn-) and Oxides (Mox) Where M= Chromium, Molybdenum, Tungsten, Vanadium, Niobium and Tantalum. *J. Phys. Chem.* **1987**, *91* (18), 4779–4788.

(63)   Yeh, J. J.; Lindau, I. Atomic Subshell Photoionization Cross Sections and Asymmetry Parameters: 1 [Less-than-or-Equals, Slant] Z [Less-than-or-Equals, Slant] 103. *At. Data Nucl. Data Tables* **1985**, *32* (1), 1–155.

(64)   Savory, C. N.; Ganose, A. M.; Travis, W.; Atri, R. S.; Palgrave, R. G.; Scanlon, D. O. An Assessment of Silver Copper Sulfides for Photovoltaic Applications: Theoretical and Experimental Insights. *J. Mater. Chem. A* **2016**, *4* (32), 12648–12657.

(65)   Bhachu, D. S.; Moniz, S. J. A.; Sathasivam, S.; Scanlon, D. O.; Walsh, A.; Bawaked, S. M.; Mokhtar, M.; Obaid, A. Y.; Parkin, I. P.; Tang, J.; et al. Bismuth Oxyhalides: Synthesis, Structure and Photoelectrochemical Activity. *Chem. Sci.* **2016**, *7* (8), 4832–4841.

(66)   Marchand, P.; Sathasivam, S.; Williamson, B. A. D.; Pugh, D.; Bawaked, S. M.; Basahel, S. N.; Obaid, A. Y.; Scanlon, D. O.; Parkin, P.; Carmalt, C. J. A Single-Source Precursor Approach to Solution Processed Indium Arsenide Thin Films †. *J. Mater. Chem. C* **2016**.

(67)   Sathasivam, S.; Arnepalli, R. R.; Bhachu, D. S.; Lu, Y.; Buckeridge, J.; Scanlon, D. O.; Kumar, B.; Singh, K. K.; Visser, R. J.; Blackman, C. S. Single Step Solution Processed GaAs Thin Films from GaMe3 and T BuAsH2 under Ambient Pressure. *J. Phys. Chem. C* **2016**, *120* (13), 7013–7019.

(68)   Treichel, H.; Mitwalsky, A.; Tempel, G.; Zorn, G.; Kern, W.; Sandier, N.; Lane, A. P. Deposition, Annealing, and Characterization of Tantalum Pentoxide Films. In *MRS Proceedings*; Cambridge Univ Press, 1992; Vol. 282, p 557.

(69)   Sahu, B. R.; Kleinman, L. Theoretical Study of Structural and Electronic Properties of B− Ta 2 O 5 and Δ− Ta 2 O 5. *Phys. Rev. B* **2004**, *69* (16), 165202.

(70)   Lee, J.; Lu, W.; Kioupakis, E. Electronic Properties of Tantalum Pentoxide Polymorphs from First-Principles Calculations. *Appl. Phys. Lett.* **2014**, *105*

(20), 202108.

(71)   Kim, J.; Magyari- Köpe, B.; Lee, K.; Kim, H.; Lee, S.; Nishi, Y. Electronic Structure and Stability of Low Symmetry Ta2O5polymorphs. *Phys. status solidi (RRL)-Rapid Res. Lett.* **2014**, *8* (6), 560–565.

(72)   Kim, K.; Jordan, K. D. Comparison of Density Functional and MP2 Calculations on the Water Monomer and Dimer. *J. Phys. Chem.* **1994**, *98* (40), 10089–10094.

(73)   Preissler, N.; Bierwagen, O.; Ramu, A. T.; Speck, J. S. Electrical Transport, Electrothermal Transport, and Effective Electron Mass in Single-Crystalline In 2 O 3 Films. *Phys. Rev. B* **2013**, *88* (8), 85305.

(74)   Mills, A.; Wang, J. Simultaneous Monitoring of the Destruction of Stearic Acid and Generation of Carbon Dioxide by Self-Cleaning Semiconductor Photocatalytic Films. *J. Photochem. Photobiol. A Chem.* **2006**, *182* (2), 181–186.

(75)   Linsebigler, A. L.; Lu, G.; Yates Jr, J. T. Photocatalysis on TiO2 Surfaces: Principles, Mechanisms, and Selected Results. *Chem. Rev.* **1995**, *95* (3), 735–758.

(76)   Yamada, Y.; Kanemitsu, Y. Determination of Electron and Hole Lifetimes of Rutile and Anatase TiO2 Single Crystals. *Appl. Phys. Lett.* **2012**, *101* (13), 133907.

(77)   Leng, W. H.; Barnes, P. R. F.; Juozapavicius, M.; O'Regan, B. C.; Durrant, J. R. Electron Diffusion Length in Mesoporous Nanocrystalline TiO2 Photoelectrodes during Water Oxidation. *J. Phys. Chem. Lett.* **2010**, *1* (6), 967–972.

(78)   Sun, J.; Zhong, D. K.; Gamelin, D. R. Composite Photoanodes for Photoelectrochemical Solar Water Splitting. *Energy Environ. Sci.* **2010**, *3* (9), 1252–1261.

(79)   Pala, R. A.; Leenheer, A. J.; Lichterman, M.; Atwater, H. A.; Lewis, N. S. Measurement of Minority-Carrier Diffusion Lengths Using Wedge-Shaped Semiconductor Photoelectrodes. *Energy Environ. Sci.* **2014**, *7* (10), 3424–3430.

(80)   Santato, C.; Ulmann, M.; Augustynski, J. Enhanced Visible Light Conversion Efficiency Using Nanocrystalline WO3 Films. *Adv. Mater.* **2001**, *13* (7), 511–514.

(81)   Rico, V.; Borrás, A.; Yubero, F.; Espinós, J. P.; Frutos, F.; González-Elipe, A. R. Wetting Angles on Illuminated Ta2O5 Thin Films with Controlled Nanostructure. *J. Phys. Chem. C* **2009**, *113* (9), 3775–3784.

TOC graphic